

# Dislocation controlled formation and kinetics of grain boundary loops in two-dimensional crystals

François A. Lavergne<sup>a</sup>, Arran Curran<sup>a</sup>, Dirk G. A. L. Aarts<sup>a</sup>, and Roel P. A. Dullens<sup>a,1</sup>

<sup>a</sup>Department of Chemistry, Physical and Theoretical Chemistry Laboratory, University of Oxford, South Parks Road, Oxford OX1 3QZ, United Kingdom

This manuscript was compiled on May 3, 2018

**The formation and kinetics of grain boundaries are closely related to the topological constraints imposed on their complex dislocation structure. Loop-shaped grain boundaries are unique structures to establish such a link because their overall topological “charge” is zero due to their null net Burgers vector. Here, we observe that a local rotational deformation of a two-dimensional colloidal crystal with an optical vortex only results in a grain boundary loop if the product of its radius and misorientation exceeds a critical value. Above this value, the deformation is plastic and the grain boundary loop spontaneously shrinks at a rate that solely depends on this product while otherwise, the deformation is elastically restored. We show that this elastic-to-plastic crossover is a direct consequence of the unique dislocation structure of grain boundary loops. At the critical value, the loop is structurally equivalent to the so called “flower defect” and the shrinkage rate diverges. Our results thus reveal a new general limit on the formation of grain boundary loops in two-dimensional crystals and elucidate the central role of defects in both the onset of plasticity and the kinetics of grain boundaries.**

Grain boundaries | colloids | dislocations | optical tweezing

A grain boundary (GB) loop in a two-dimensional crystal is a GB that closes onto itself. It thereby encloses a patch of crystal rotated with respect to the outer crystal by an angle called the misorientation (1–3). The disruption of crystalline order at a GB is marked by the presence of crystalline defects called dislocations along the GB line (3), so that a GB loop can also be seen as a closed line of dislocations (1, 2). GB loops exhibit fascinating properties due to their closed shape. For example, GB loops of different shapes but enclosing equal initial areas shrink within the same amount of time, due to curvature-dependent capillary forces (4). The area  $A$  enclosed by the GB loop decreases at a constant rate according to

$$\frac{dA}{dt} = -2\pi M^*, \quad [1]$$

where  $M^*$  is the reduced mobility (4, 5). Another remarkable feature is the variety and symmetry of the arrangement of dislocations along GB loops (1). In hexagonal lattices, a dislocation consists of two neighbouring 5- and 7-coordinated sites and introduces a lattice distortion characterised by a Burgers vector of length equal to the lattice spacing, that is oriented along one of the six crystallographic directions (6–8). When six of these dislocations arrange into a loop, they form the so-called “flower defect”, which has a low energy cost per dislocation (1). Owing to their null net Burgers vector, grain boundary loops are reported to play a role in defect-mediated ordering and disordering processes like stress relaxation in crystals (9) and topological phase transitions such as two-dimensional melting (10, 11).

Despite their apparent simplicity, GB loops can significantly impact various properties of two-dimensional materials (1, 8)

such as the thermal conductivity of graphene (12). While the engineering of GB loops is a promising route to tune the properties of two-dimensional materials, many aspects of their formation, kinetics, and their link to the dislocation structure are still elusive. In fact, qualitatively different results on how the reduced mobility depends on the misorientation (13–15) and on the initial size of the GB loop (15, 16) have been found in simulations, together with anomalies in the shrinkage kinetics compared to Eq. (1) (17, 18). While the creation of GB loops and their shrinkage driven by electron irradiation has been recently achieved in graphene (2, 19), systematic studies of the kinetics and dislocation structure of GB loops as a function of the misorientation remain challenging in these systems.

Here, we exploit the inherent softness of colloidal crystals and manipulate them using optical vortices to create GB loops on demand, with a well-defined misorientation and size. The obtained colloidal GB loops shrink *spontaneously* in contrast to GB loops in graphene, which are stable due to the strong covalent bonding (20). The conveniently accessible length and time scales of colloidal crystals (21–29) allow us to directly visualise the time-resolved shrinkage kinetics and dislocation structure of GB loops in two-dimensional hexagonal lattices.

## Creation of grain boundary loops

The GB loops are created by rotating a circular portion of a two-dimensional colloidal crystal (inner grain) counter-clockwise with an optical vortex generated by holographic optical tweezing as shown in Fig. 1(a)–(c) (30–32) (for details,

### Significance Statement

Twisting a circular patch inside a large crystal does not always lead to a bicrystal. This is due to the topological properties of the resulting loop-shaped grain boundaries and the defects they are made of. By deforming a crystalline monolayer of colloidal particles using optical tweezers, we find that the product of the angle of rotation and the size of the patch needs to exceed a universal value that only depends on the lattice type for a grain boundary loop to form, while otherwise, the deformation is elastically restored. We measure this universal value from the shrinkage kinetics of grain boundary loops and relate it to the complex dislocation structure and reactions, which we directly visualise in our experiments.

F.A.L. and R.P.A.D. designed the research. A.C. developed the optical tweezing stage and protocols. F.A.L. and A.C. performed the experiments. F.A.L. analysed the data. F.A.L., A.C., D.G.A.L.A. and R.P.A.D. interpreted the results. F.A.L. and R.P.A.D. wrote the manuscript and all authors commented on the manuscript.

The authors declare no conflict of interest.

<sup>1</sup>To whom correspondence should be addressed. E-mail: roel.dullens@chem.ox.ac.uk

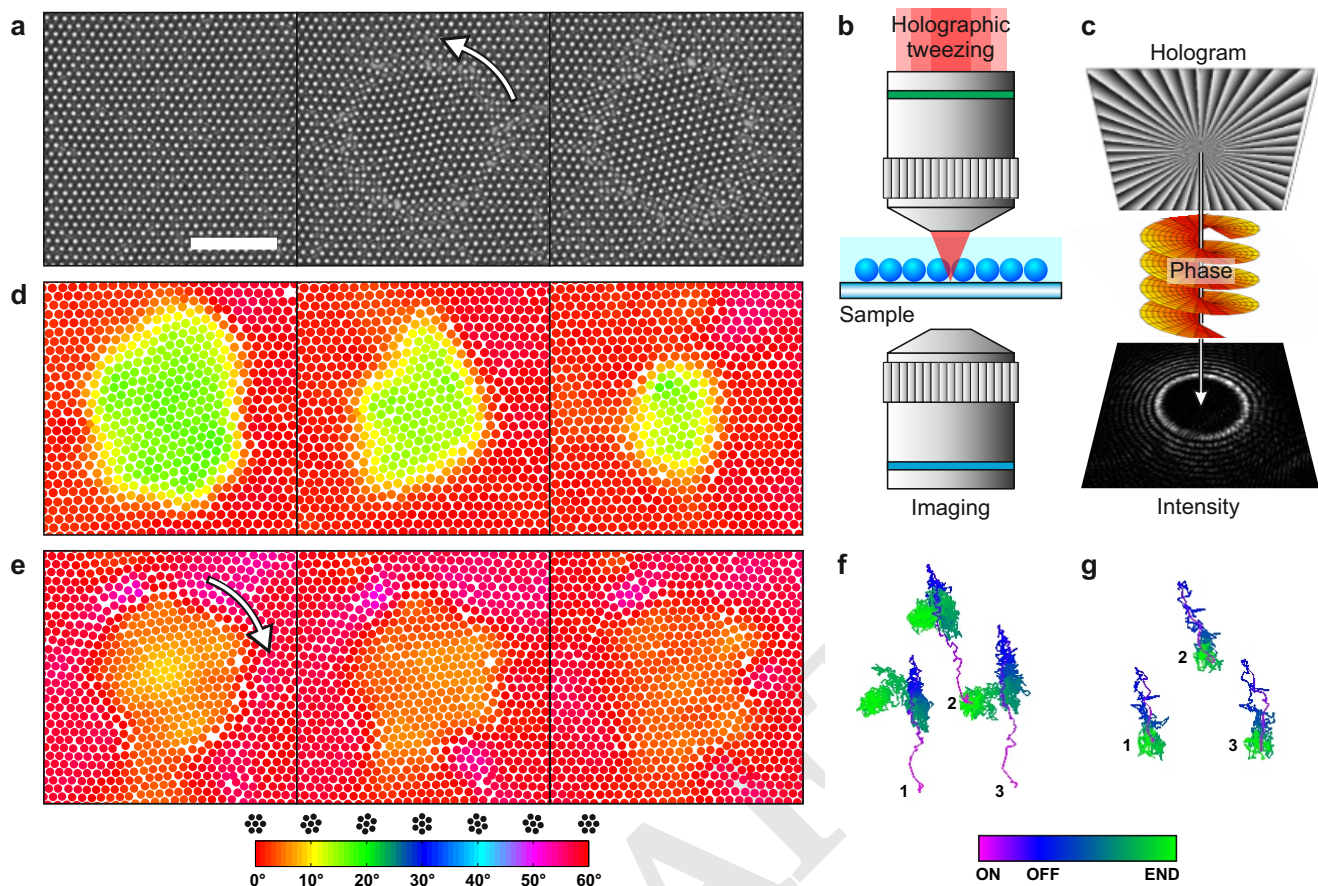


**Fig. 1. Grain boundary loop formation and elastic-to-plastic deformation crossover.** **a**, Creation of a grain boundary loop in a colloidal crystal by rotation of a circular grain counter-clockwise (arrow) using an optical vortex. Scale bar, 25  $\mu\text{m}$ . **b**, Schematic of the sample cell containing the two-dimensional colloidal crystal, mounted on a holographic optical tweezing and video-microscopy setup. **c**, Schematic of the hologram, phase front, intensity profile and direction of propagation of the optical vortex used to create the grain boundary loop. **d**, Shrinkage of a grain boundary loop of initial misorientation  $\theta_0 > \theta^c$ , after the vortex is turned off. The local crystal orientation is indicated by the colourbar. **e**, Same as in **d** in the case  $\theta_0 < \theta^c$ , where the deformation is restored by grain rotation clockwise (arrow). **f**, Representative particle trajectories (labelled 1, 2 and 3) colour-coded according to the time elapsed during the exposure to the vortex (period ON to OFF on the colourbar) and the subsequent evolution of the grain (period OFF to END on the colourbar) in the case of plastic deformation ( $\theta_0 > \theta^c$ ). **g**, Same as in **f** but now in the case of elastic deformation ( $\theta_0 < \theta^c$ ).

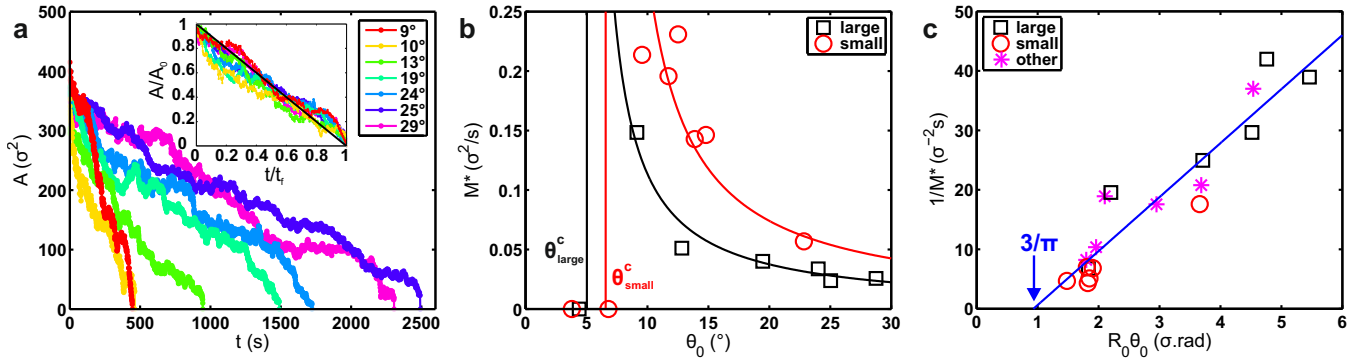
see SI). The inner grain rotates as long as the vortex is applied (Movie S1). When the desired misorientation is reached the vortex is turned off and the inner grain is then free from external forces. The subsequent evolution of the GB loop is then monitored using optical video-microscopy (33) (Movie S1). The initial misorientation,  $\theta_0$ , is varied from  $0^\circ$  to  $30^\circ$ , which is the maximum misorientation in a hexagonal crystal, and the initial radius,  $R_0$ , lies within the range  $8\sigma - 11\sigma$ , where  $\sigma$  is the lattice spacing. Crucially, the use of optical vortices enables us to create relatively large GB loops in comparison to a previously used approach based on single particle trapping (32). Moreover, a recently developed method based on “optical blasting” (34) enables the creation of arbitrarily shaped GB loops but without control of the misorientation, which is a key parameter in the structural stability and kinetics of GB loops.

Figure 1(d) shows the crystal orientation maps (for details see SI) corresponding to the evolution of a GB loop with  $\theta_0 = 16.4^\circ$  and  $R_0 = 10.3\sigma$  after the vortex is turned off. For this relatively large initial misorientation, a GB loop is obtained, which then spontaneously *shrinks* until a single crystal is left (Movie S1). The trajectories of the particles

confirm that after complete shrinkage, they are located at different lattice sites than before the deformation (Fig. 1(f)). This irreversibility indicates that the deformation induced by the vortex is *plastic*. Surprisingly, when we repeat the experiment with a misorientation of  $\theta_0 = 4.5^\circ$ , the grain merely *rotates* back clockwise with a *fixed* radius, until merging with the outer crystal (Fig. 1(e)). The trajectories of the particles clearly confirm that they return to their original crystal sites (Fig. 1(g)). This reversibility shows that the deformation is *elastic* in this case. These observations thus show that for a given  $R_0$ , there is a critical value of the initial misorientation,  $\theta^c$ , which marks a crossover between plastic deformation followed by shrinkage for  $\theta_0 > \theta^c$ , and elastic deformation followed by rotation at constant radius for  $\theta_0 < \theta^c$ .

### Kinetics of shrinkage

We now characterise the shrinkage kinetics of the GB loops created by plastic deformation ( $\theta_0 > \theta^c$ ). To this end, we monitor the time-evolution of the area  $A = \pi R^2$  of GB loops (for details see SI) with  $R_0 = 10.8 \pm 0.5\sigma$  for initial misorien-



**Fig. 2. Shrinkage kinetics of grain boundary loops.** **a**, Time evolution of the area  $A$  enclosed by equally sized grain boundary loops ( $R_0 = 10.8 \pm 0.5\sigma$ ) of different initial misorientations  $\theta_0$ . Data collapse of  $A/A_0$  as a function of the rescaled time  $t/t_f$  (inset). **b**, The reduced mobility  $M^*$  as a function of the initial misorientation  $\theta_0$  for large ( $R_0 = 10.8 \pm 0.5\sigma$ ) and small ( $R_0 = 8.4 \pm 0.8\sigma$ ) grain boundary loops. Below  $\theta^c$ ,  $M^*$  is set to 0 by convention. **c**, Data collapse of  $1/M^*$  as a function of  $R_0\theta_0$ . The data comprise large, small, and other sized grain boundary loops. The critical value where  $M^*$  diverges corresponds to the vertical asymptotes in **b**, which match the onsets of plastic deformation for large and small grain boundary loops, located at  $\theta_{large}^c$  and  $\theta_{small}^c$ . The value of  $3/\pi$  corresponds to the critical value for  $R\theta$  as given by Eq. (3).

tations  $\theta_0$  in the range  $9^\circ - 28^\circ$  (Fig. 2(a)), well above the critical value  $\theta^c \simeq 5^\circ$  for this  $R_0$ . In all cases,  $A(t)$  decreases monotonically and, importantly, it is clearly observed that the higher the initial misorientation, the longer the shrinkage takes. To test whether the GB loop shrinks at constant rate, we integrate Eq. (1) as  $A/A_0 = 1 - t/t_f$ , where the total shrinkage time,  $t_f = A_0/(2\pi M^*)$ , is directly measured from the data in Fig. 2(a). Plotting  $A/A_0$  versus  $t/t_f$  shows a good collapse of the data (inset of Fig. 2(a)), which indicates that the shrinkage occurs at a constant rate and is thus effectively characterised by a *single* kinetic coefficient, the reduced mobility  $M^*$ . Its variation as a function of the initial misorientation  $\theta_0$  is shown in Fig. 2(b), where it can be seen that  $M^*$  decreases upon increasing initial misorientation, consistent with Fig. 2(a). This trend is particularly notable as it is the opposite of the behaviour commonly observed in atomistic simulations of circular grains (13, 14). Note that in the elastic regime characterised by pure grain rotation ( $\theta_0 < \theta^c$ ), we set  $M^* = 0$  by convention (Fig. 2(b)).

To investigate the role of the initial radius of the GB loop, the same experiments and analyses were repeated for a set of smaller GB loops with  $R_0 = 8.4 \pm 0.8\sigma$ , see Fig. 2(b). For this set of smaller GB loops we find a higher critical value of  $\theta^c \simeq 7^\circ$  (Movie S2). Secondly, the  $M^*$  of smaller GB loops is generally higher than that of larger GB loops with the same initial misorientation, while the trend as a function of  $\theta_0$  remains the same. In other words, the  $M^*$  of GBs loops is enhanced by their initial curvature. As such, one expects the  $M^*$  of a GB loop to be higher than that of a *flat* GB with the same misorientation. Indeed, a GB loop with  $R_0 \simeq 11\sigma$  and  $\theta_0 = 19^\circ$  has  $M^* \simeq 0.05\sigma^2/s$  (Fig. 2(b)), i.e.  $3.6 \times 10^{-13} m^2/s$ , which is significantly higher than  $M_{flat}^* = 1.3 \times 10^{-13} m^2/s$  for a flat GB with misorientation  $20^\circ$  in the exact same colloidal system (35). Crucially, our results thus show that the kinetic properties of GBs strongly depend on their geometry.

Having established that the reduced mobility depends on both the initial misorientation and initial radius of the GB loop, we now seek to find a single variable that determines the value of the reduced mobility of GB loops. As suggested in (15), we plot  $1/M^*$  as a function of the product  $R_0\theta_0$  in the regime of shrinkage following plastic deformation ( $\theta_0 > \theta^c$ ) in

Fig. 2(c). The data points comprise both the set of large and small GB loops, together with other GB loops that do not fall into either of these two classes. A good collapse onto a master line with a *positive*  $x$ -intercept is obtained, showing that the reduced mobility solely depends on  $R_0\theta_0$  according to

$$\frac{1}{M^*} = K(R_0\theta_0 - [R\theta]^c), \quad [2]$$

where  $K$  is a constant. This implies that the kinetics of GB loops is determined by their initial state, i.e. two GB loops with identical values of  $R_0\theta_0$  shrink at the same rate. While the linear behaviour of  $1/M^*$  versus  $R_0\theta_0$  was reported in (15), no intercept was observed in the simulations nor theoretically predicted. Importantly, the positive  $x$ -intercept at the critical value,  $[R\theta]^c \simeq 0.93\sigma$  in Fig. 2(c), shows the existence of a lower bound on  $R_0\theta_0$ , corresponding to a divergence of the reduced mobility,  $M^* \rightarrow +\infty$ . Plotting Eq. (2) in Fig. 2(b) reveals that the observed values of  $\theta^c$  are in excellent agreement with the vertical asymptotes located at  $\theta^c = [R\theta]^c/R_0$ , consistent with the observed decrease of  $\theta^c$  with increasing  $R_0$ . Crucially, this shows that the divergence of  $M^*$  is a dynamic signature of the crossover between elastic and plastic deformation. Such a crossover has never been probed in simulations as  $R_0$  is typically too large, leading to  $\theta^c \rightarrow 0$  (13–15), nor in experiments where there has been little control over  $\theta_0$  (2, 19, 34).

### Dislocation origin of grain boundary loop formation

Next, we show that the existence of the lower bound on  $R_0\theta_0$  directly originates from geometrical constraints on the dislocation structure of GB loops imposed by their closed shape. In general, the sum of the Burgers vectors of dislocations located on a given portion of GB is oriented along its normal direction (3, 36). The simplest configuration compatible with this constraint is a portion of a GB containing dislocations with identical Burgers vectors all oriented along the normal direction and separated by a distance  $\sigma/\theta$  (3, 8) (Fig. 3(a)). This situation occurs when this portion of GB is perpendicular to one of the six possible Burgers vectors of the hexagonal lattice, i.e. perpendicular to one of the six crystallographic directions (3, 6–8). For a GB loop, however, the normal rotates by  $2\pi$  along the loop and goes through all six directions



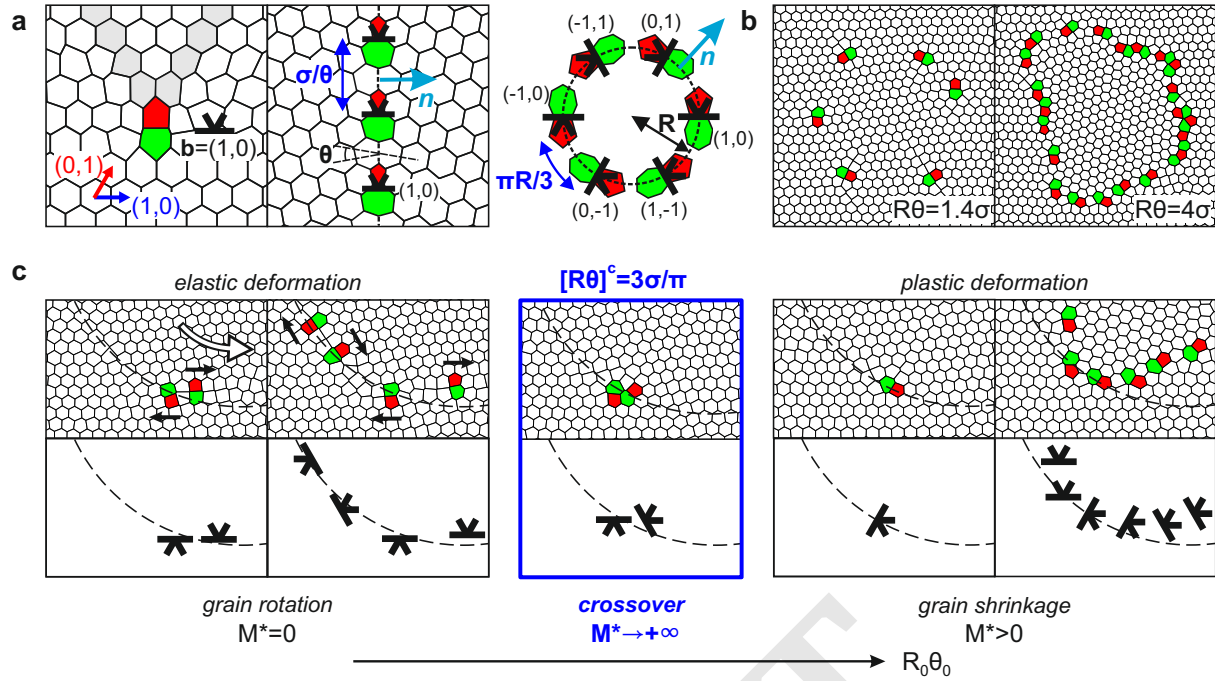


**Fig. 3. Dislocation origin of elastic-to-plastic deformation crossover.** **a.** (Left) Schematic view of an isolated dislocation induced by the insertion of two semi-infinite crystal lines (grey) with its Burgers vector  $\vec{b}$  expressed in crystal coordinates (blue and red arrows). (Middle) Schematic of the simplest flat GB configuration, which contains identical dislocations with their Burgers vectors along the normal to the GB ( $\vec{n}$ ) and spaced by  $\sigma/\theta$ . (Right) Schematic of the simplest GB loop configuration, which consists of six equally spaced dislocations with their Burgers vectors along the local normal ( $\vec{n}$ ). **b.** Examples of GB loops obtained in the experiments, with  $R\theta$  near (left) and well above (right)  $[R\theta]^c$ . **c.** (Left) Local view of a portion of GB loop (dashed line) during rotation of the grain by the optical vortex (white arrow). The dislocation structure is shown in the elastic regime ( $R_0\theta_0 < [R\theta]^c$ , left), at the crossover ( $R_0\theta_0 = [R\theta]^c$ , middle), and in the plastic regime ( $R_0\theta_0 > [R\theta]^c$ , right).

of the Burgers vectors at least once (Fig. 3(a)). This implies that the minimum number of dislocations around a GB loop is six. This configuration can be interpreted as a GB loop consisting of six portions of GB, each with length  $\pi R/3$  and containing one dislocation. For such a configuration to exist, the dislocation spacing imposed by the misorientation,  $\sigma/\theta$ , must thus be smaller than  $\pi R/3$ , which implies that

$$R\theta \geq \frac{3}{\pi}\sigma. \quad [3]$$

This represents a general lower bound on the product of the radius and the misorientation of a GB loop, which also applies to its value in the initial state,  $R_0\theta_0$ .

Interestingly, the lower bound predicted in Eq. (3) corresponds to an infinite family of GB loops with  $R\theta = 3\sigma/\pi$ , one of which is structurally equivalent to the flower defect ( $\theta = \pi/6$ ) observed in graphene (1, 2, 12). This lower bound is also in remarkably good agreement with the experimental value of  $0.93\sigma$  corresponding to the elastic-to-plastic crossover, i.e.  $[R\theta]^c = 3\sigma/\pi$  (Fig. 2(c)). To illustrate that Eq. (3) applies to any time during shrinkage, we show two experimental GB loops with their  $R\theta$  values in Fig. 3(b). In the first case,  $R\theta$  is larger but close to  $[R\theta]^c$ , so that the GB loop consists of six roughly equally spaced dislocations, reminiscent of the flower-defect family. In the second case,  $R\theta$  is well above  $[R\theta]^c$ , so that the GB loop is composed of many closely spaced dislocations.

We now elucidate how the elastic-to-plastic crossover originates from the dislocation structure of GB loops. In the case of elastic deformation, the initial misorientation of a GB loop

with a given initial size is so small that Eq. (3) is violated, i.e.  $R_0\theta_0 < 3\sigma/\pi$ . Therefore the dislocation spacing  $\sigma/\theta$  is larger than  $\pi R/3$  and as a result, no GB loop can be formed as the dislocations cannot be fitted on it. The elastic deformation is then marked by the dissociation of pairs of dislocations with opposite Burgers vectors parallel to the GB loop (Fig. 3(c)), and not perpendicular as required for a stable GB. Hence, once the vortex is turned off the inner grain rotates back simply via the glide of dislocations with opposite Burgers vectors towards each other until the original crystal is recovered. In the case of plastic deformation, the misorientation of a GB loop with a fixed size is large enough so that Eq. (3) is satisfied, i.e.  $R_0\theta_0 \geq 3\sigma/\pi$ . In this case, dislocations are created such that the sum of their Burgers vectors is locally perpendicular to the GB loop (Fig. 3(c)), hence a stable GB loop is formed. This corresponds to a plastic deformation as the original crystal can only be recovered via grain shrinkage.

It is important to stress that  $[R\theta]^c = 3\sigma/\pi$  is a general lower bound that solely stems from the hexagonal lattice structure and the loop shape of the grain boundary. It means that no GB loop with  $R\theta$  below  $3\sigma/\pi$  can be created by any continuous local deformation of any two-dimensional hexagonal crystal. In colloidal crystals, however, we have shown that this lower bound has a clear dynamic signature in that it manifests itself as a diverging reduced mobility of shrinking GB loops.

## Dislocation reactions

Finally, we show that grain shrinkage is achieved by complex dislocation reactions (13, 32) that we directly visualise



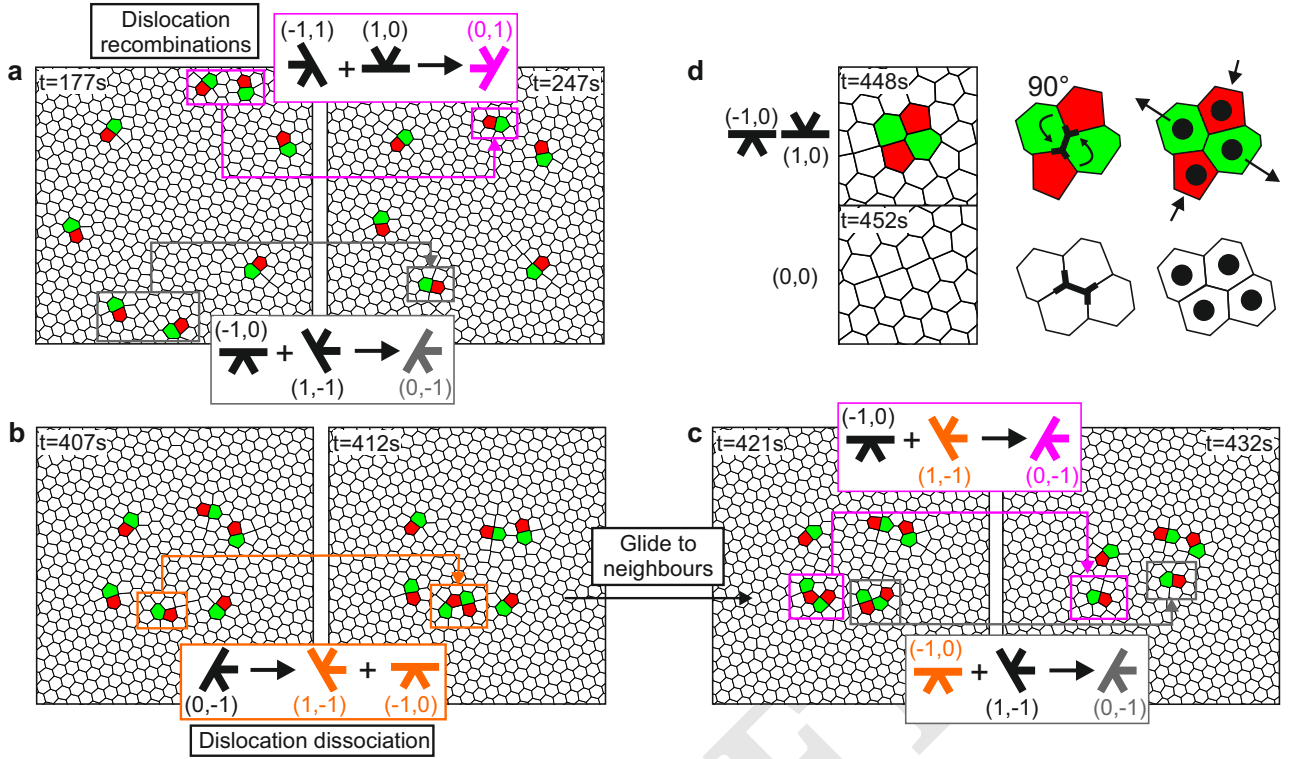


**Fig. 4. Dislocation reactions during shrinkage of grain boundary loops.** **a**, Two dislocation recombinations with the corresponding balance of Burgers vectors for a GB loop with  $R_0\theta_0 = 1.7\sigma$  (Movie S3). Time is counted from the start of shrinkage. **b**, A dislocation dissociation event followed by the glide of the products to neighbouring dislocations. **c**, Subsequent recombinations to enable further shrinkage. **d**, A dislocation pair that annihilates following a process analogous to a Stone-Wales transformation, namely a  $90^\circ$  edge rotation in the Voronoi diagram, which is achieved by small antiparallel particle displacements.

for a GB loop with  $R_0\theta_0 = 1.7\sigma$  in Fig. 4 and Movie S3. Dislocation reactions must preserve the total Burgers vector  $\sum_i \vec{b}_i$  while lowering the elastic strain energy (7, 13, 32). We first observe that the number of dislocations along the GB loop can be reduced by a so-called *dislocation recombination* (Fig. 4(a), Movie S4). For two neighbouring dislocations with  $|\vec{b}_1| = |\vec{b}_2| = \sigma$  and  $|\vec{b}_1 + \vec{b}_2| > \sigma$ , as it is the case for the “flower defect”-like configuration in Fig. 4(a), recombinations do not occur due to the large increase in the elastic strain energy. Instead, we observe a second process consisting of a dislocation *dissociation* (Fig. 4(b), Movie S5) and two subsequent recombinations between the dislocations resulting from the dissociation and their neighbouring dislocations (Fig. 4(c)). Note that dislocations can meet their neighbours by *glide*, which is the motion of dislocations parallel to their Burgers vector (7). Similar dislocation reactions occur until a defect structure corresponding to a pair of dislocations with opposite Burgers vectors, analogous to the Stone-Wales defect in graphene (20, 37, 38), is reached (Fig. 4(d)). The perfect crystal is recovered by a third elementary process, reminiscent of the Stone-Wales transformation (20, 39), namely a simple edge rotation of  $90^\circ$  in the Voronoi diagram (Fig. 4(d)), topologically equivalent to the bond rotation in graphene (20, 37–39). While in graphene this is energetically very costly (20), in our colloidal crystal it simply corresponds to the two 5-fold coordinated (7-fold coordinated) particles moving towards (away from) each other, as illustrated in Fig. 4(e). This shows how

very small particle displacements in colloidal crystals lead to topological changes in the lattice to recover the original perfect crystal. Crucially, despite this rather complex pathway, we have shown that the rate of shrinkage  $M^*$  solely depends on  $R_0\theta_0$ , thus demonstrating that the kinetics of GB loops is fully determined by their *initial* dislocation configuration.

## Conclusions

Our results highlight the intimate relation between the formation and kinetics of grain boundary loops in two-dimensional colloidal crystals and their unique dislocation structure. In particular, we identify a fundamental limit to grain boundary loop formation in two-dimensional crystals and thereby uncover the dislocation origin of the crossover between elastic and plastic deformation of a crystal by rotation. We also show that the shrinking kinetics of grain boundary loops is fully determined by their initial dislocation structure, as quantified by the product of their initial size and misorientation. We believe that our results on the topology of grain boundary loop formation in relation to their dislocation structure in hexagonal colloidal crystals are relevant to other two-dimensional materials with mathematically dual structures (8, 40–42). In addition, controlling the formation and kinetics of grain boundary loops may help in engineering the grain boundary loop content and thereby the properties of these materials.

**ACKNOWLEDGMENTS.** We thank Paul Chaikin and Lucio Isa for useful discussions. The European Research Council (ERC) is acknowledged for financial support (ERC Starting Grant 279541-IMCOLMAT).

- Cockayne E et al. (2011) Grain boundary loops in graphene. *Phys. Rev. B* 83:195425.
- Gong C, He K, Chen Q, Robertson AW, Warner JH (2016) In situ high temperature atomic level studies of large closed grain boundary loops in graphene. *ACS Nano* 10(10):9165–9173.
- Howe JM (1997) *Interfaces in materials: atomic structure, thermodynamics and kinetics of solid-vapor, solid-liquid and solid-solid interfaces*. (Wiley-Interscience).
- Mullins WW (1956) Two-dimensional motion of idealized grain boundaries. *Journal of Applied Physics* 27(8).
- Lobkovsky AE, Karma A, Mendelev MI, Haataja M, Srolovitz DJ (2004) Grain shape, grain boundary mobility and the Herring relation. *Acta Materialia* 52(2):285–292.
- Hull D, Bacon DJ (2001) *Introduction to dislocations*. (Butterworth-Heinemann).
- Nelson DR (2002) *Defects and geometry in condensed matter physics*. (Cambridge University Press).
- Yazyev OV, Chen YP (2014) Polycrystalline graphene and other two-dimensional materials. *Nature Nanotechnology* 9:755 – 767.
- van der Meer B et al. (2014) Highly cooperative stress relaxation in two-dimensional soft colloidal crystals. *Proceedings of the National Academy of Sciences* 111(43):15356–15361.
- Saito Y (1982) Monte carlo studies of two-dimensional melting: Dislocation vector systems. *Phys. Rev. B* 26:6239–6253.
- Fisher DS, Halperin BI, Morf R (1979) Defects in the two-dimensional electron solid and implications for melting. *Phys. Rev. B* 20:4692–4712.
- Khosravi N et al. (2013) Effects of a grain boundary loop on the thermal conductivity of graphene: A molecular dynamics study. *Computational Materials Science* 79:132 – 135.
- Trautt ZT, Mishin Y (2012) Grain boundary migration and grain rotation studied by molecular dynamics. *Acta Materialia* 60(5):2407–2424.
- Wu KA, Voorhees PW (2012) Phase field crystal simulations of nanocrystalline grain growth in two dimensions. *Acta Materialia* 60(1):407–419.
- Adland A, Xu Y, Karma A (2013) Unified theoretical framework for polycrystalline pattern evolution. *Physical Review Letters* 110:265504.
- Upmanyu M, Srolovitz D, Lobkovsky A, Warren J, Carter W (2006) Simultaneous grain boundary migration and grain rotation. *Acta Materialia* 54(7):1707 – 1719.
- Vega DA et al. (2005) Ordering mechanisms in two-dimensional sphere-forming block copolymers. *Physical Review E* 71:061803.
- Bernstein N (2008) The influence of geometry on grain boundary motion and rotation. *Acta Materialia* 56(5):1106 – 1113.
- Kurasch S et al. (2012) Atom-by-atom observation of grain boundary migration in graphene. *Nano Letters* 12(6):3168–3173.
- Li L, Reich S, Robertson J (2005) Defect energies of graphite: Density-functional calculations. *Phys. Rev. B* 72:184109.
- Nagamanasa KH, Gokhale S, Ganapathy R, Sood AK (2011) Confined glassy dynamics at grain boundaries in colloidal crystals. *Proceedings of the National Academy of Sciences* 108(28):11323–11326.
- Gokhale S, Nagamanasa KH, Santhosh V, Sood AK, Ganapathy R (2012) Directional grain growth from anisotropic kinetic roughening of grain boundaries in sheared colloidal crystals. *Proceedings of the National Academy of Sciences* 109(50):20314–20319.
- Gokhale S, Nagamanasa KH, Ganapathy R, Sood AK (2013) Grain growth and grain boundary dynamics in colloidal polycrystals. *Soft Matter* 9:6634–6644.
- Lavergne FA, Aarts DGAL, Dullens RPA (2015) Determining local geometrical features of grain boundaries from microscopy. *Journal of Physics: Condensed Matter* 27(19):194117.
- Deuschländer S, Dillmann P, Maret G, Keim P (2015) Kibble-Zurek mechanism in colloidal monolayers. *Proceedings of the National Academy of Sciences* 112(22):6925–6930.
- Li B et al. (2016) Modes of surface premelting in colloidal crystals composed of attractive particles. *Nature* 531(7595):485–488.
- Lin NY, Bierbaum M, Schall P, Sethna JP, Cohen I (2016) Measuring nonlinear stresses generated by defects in 3D colloidal crystals. *Nature Materials*.
- Thorneywork AL, Abbott JL, Aarts DGAL, Dullens RPA (2017) Two-dimensional melting of colloidal hard spheres. *Phys. Rev. Lett.* 118(15):158001.
- Lavergne FA, Aarts DGAL, Dullens RPA (2017) Anomalous grain growth in a polycrystalline monolayer of colloidal hard spheres. *Phys. Rev. X* 7:041064.
- Irvine ER, Spalding GC, Dearing MT, Sheets SA, Grier DG (2001) Computer-generated holographic optical tweezer arrays. *Review of Scientific Instruments* 72(3).
- Grier DG (2003) A revolution in optical manipulation. *Nature* 424(6950):810–816.
- Irvine WTM, Hollingsworth AD, Grier DG, Chaikin PM (2013) Dislocation reactions, grain boundaries, and irreversibility in two-dimensional lattices using topological tweezers. *Proceedings of the National Academy of Sciences of the United States of America* 110(39):15544–15548.
- Crocker JC, Grier DG (1996) Methods of digital video microscopy for colloidal studies. *Journal of Colloid and Interface Science* 179(1):298–310.
- Cash CE et al. (2018) Local melting attracts grain boundaries in colloidal polycrystals. *Phys. Rev. Lett.* 120:018002.
- Skinner TOE, Aarts DGAL, Dullens RPA (2010) Grain-boundary fluctuations in two-dimensional colloidal crystals. *Physical Review Letters* 105:168301.
- Frank FC (1950) Report of the symposium on the plastic deformation of crystalline solids. *Carnegie Institute of Technology, Pittsburgh* pp. 150–154.
- Stone A, Wales D (1986) Theoretical studies of icosahedral c60 and some related species. *Chemical Physics Letters* 128(5):501 – 503.
- Cockayne E (2012) Graphing and grafting graphene: Classifying finite topological defects. *Phys. Rev. B* 85:125409.
- Kotakoski J et al. (2011) Stone-wales-type transformations in carbon nanostructures driven by electron irradiation. *Phys. Rev. B* 83:245420.
- Rivier N, Miri M, Oguey C (2005) Plasticity and topological defects in cellular structures: Extra matter, folds and crab moulting. *Colloids and Surfaces A: Physicochemical and Engineering Aspects* 263(1):39 – 45.
- Lin Y, Connell JW (2012) Advances in 2D boron nitride nanostructures: nanosheets, nanoribbons, nanomeshes, and hybrids with graphene. *Nanoscale* 4:6908–6939.
- Choi J, Huh J, Carter KR, Russell TP (2016) Directed self-assembly of block copolymer thin films using minimal topographic patterns. *ACS Nano* 10(8):7915–7925. PMID: 27391372.